Tribology International 62 (2013) 1–7

Contents lists available at SciVerse ScienceDirect

Tribology International

journal homepage: www.elsevier.com/locate/triboint

Obtaining the pressure spike and maximum shear stress from optical interferometry data

N. Biboulet [a], P. Sperka [b,c], C.H. Venner [d], A.A. Lubrecht [a,*], I. Krupka [b,c]

[a] Université de Lyon, INSA-Lyon, LaMCoS, CNRS UMR 5259, Villeurbanne F69621, France
[b] Brno University of Technology, Technicka 2896/2, 616 69 Brno, Czech Republic
[c] CEITEC BUT, Brno University of Technology, Technicka 2896/2, 616 69 Brno, Czech Republic
[d] University of Twente, CWT, The Netherlands

ARTICLE INFO

Article history:
Received 12 September 2012
Received in revised form
10 January 2013
Accepted 13 January 2013
Available online 4 February 2013

Keywords:
EHL
Optical interferometry
Pressure spike
Shear stress

ABSTRACT

In order to predict and optimise highly loaded contact performance, accurate lubricant data is crucial. The lubricant's high-pressure rheological behaviour is by far the least known parameter. However, this is the key factor to realistic modeling of non-Newtonian Elasto-Hydrodynamic lubrication. In this paper a new approach is described to extract such data from optical interferometric film thickness measurements of EHL contacts. The approach is relatively straightforward and cheap compared to "out of contact" rheological experiments using specialized equipment.

A measured high-resolution film thickness distribution was positioned using a computed film thickness distribution as a reference. The reference is computed using the same operating conditions as the measurement. Subsequently, from the computed film thickness difference, a pressure difference file is obtained by deconvolution. Adding this pressure difference to the computed pressure file associated with the computed reference film thickness, provides a corrected pressure distribution, as it has appeared in the experimental contact. In this paper results are presented for the pressure spike region of the contact, in which significant shear stresses occur. The basic approach and its difficulties are described as well as some "tricks", such as the reduction of (local) noise resulting from the ill-posedness of the deconvolution. It is shown that simple averaging over a circle segment in the pressure spike zone, results in significant noise reduction and a very good 'measured' pressure spike.

1. Introduction

The investigation of the high pressure rheological properties of liquids/lubricants has been an important topic of study in the physical and tribological research community for almost a century, see [1,2]. Understanding the high pressure behaviour of lubricants is of crucial importance for accurate modeling and prediction of the behaviour of elasto-hydrodynamically lubricated contacts. As a result of various trends in design (down sizing, increased efficiency), the operating conditions are becoming increasingly severe. Higher loads and higher temperatures, lead to thinner films, with increasing importance of small scale effects such as asperity deformation, and with local film break down and re-formation. Accurate prediction of EHL contact behaviour in extreme cases requires an increased understanding of the flow behaviour on an increasingly small scale. A prerequisite for modeling the relevant phenomena are accurate and validated models describing the rheological behaviour, i.e. the relation between shear stress and shear rate under the *local* conditions inside an EHL contact.

In the past decades two approaches have been used to obtain high pressure rheological data, and the matter has been the topic of rather intense debates. On the one hand, dedicated equipment has been built, i.e. high pressure viscometers and high pressure chambers [2–4]. The advantage of obtaining rheological data independently from out of contact measurements is obvious. However, such experiments are expensive to set up and not easily available. Also, the conditions in EHL contacts are rather unique so it is not obvious that the measured behaviour will be characteristic for the local situation in the contact. Alternatively, measurements of characteristic parameters such as friction or film thickness on operating EHL contacts in a model/controlled environment have been used in combination with theoretical models. The desired parameter is then determined from fitting the model predictions to the experimental results. The fundamental problem here is that, in order to obtain the rheological information (parameter), one already assumes a particular rheological model. Hence, only when the assumed rheological model

* Corresponding author. Tel.: +33 472438224.
E-mail address: Ton.Lubrecht@insa-lyon.fr (A.A. Lubrecht).

0301-679X/$ - see front matter © 2013 Elsevier Ltd. All rights reserved.
http://dx.doi.org/10.1016/j.triboint.2013.01.018

Nomenclature

a	contact radius
d	deformation
E'	equivalent Young modulus
h	film thickness
H	dimensionless film thickness, $H = hR_x/a^2$
L	Moes parameter $L = \alpha E' \cdot ((2\eta_0 u_m)/(E'R_x))^{1/4}$
M	Moes parameter $M = w/(E'R_x^2) \cdot ((2\eta_0 u_m)/(E'R_x))^{-3/4}$
p	pressure
p_h	maximum Hertzian pressure
P	dimensionless pressure $P = p/p_h$
R_x	reduced radius of curvature in x
R_y	reduced radius of curvature in y
SRR	slide to roll ratio: $(u_2 - u_1)/u_m$
u_m	mean surface velocity $u_m = (u_1 + u_2)/2$
w	load
x	coordinate in direction of rolling
y	coordinate perpendicular to the direction of rolling
X,Y	dimensionless coordinates $X = x/a$, $Y = y/a$
α	pressure viscosity index
η	viscosity, η_0 at ambient pressure
$\overline{\eta}$	dimensionless viscosity $\overline{\eta} = \eta/\eta_0$
λ	dimensionless coefficient: $\lambda = (12\eta_0 u_m R_x^2)/(p_h a^3)$
ρ	density, ρ_0 at ambient pressure
$\overline{\rho}$	dimensionless density $\overline{\rho} = \rho/\rho_0$
τ	shear stress
τ_m	maximum centerline mid film shear stress
$\overline{\tau}$	dimensionless shear stress: $\overline{\tau} = \tau/(p_h a/R_x)$

is correct the obtained value may have any significance. Otherwise, it is not clear what it represents at all. An example of this approach is the use of traction measurements on disc-machines to determine the shear modulus. A particular case is formed by the work of Johnson and Tevaarwerk [5] as their traction machine allowed identification of the fluid rheology. Results obtained from optical interferometry film thickness measurements have also been used to yield information about lubricant rheology using dynamic and steady state configurations. Optical interferometry was introduced by [6,7] and has been further developed introducing a silica spacer layer [8] to be able to measure film thickness down to a few nanometers. Nowadays, using advanced imaging techniques, very high resolution maps of the film thickness in EHL contacts under steady state and dynamic conditions can be obtained, [9–12].

A classic way in which film thickness measurements have been used to obtain rheological information is to use the central film thickness versus speed curve together with some theoretical model to determine the viscosity pressure index. For a detailed explanation and an overview of accuracy of results obtained in this way see [13]. Another approach uses a dynamic experiment (impact) [3,4,14,15]. Both methods suffer from the drawback stated above, i.e. the dependence of what is measured on the rheological model used to fit.

A more advanced way, independent of modeling assumptions regarding the lubricant behaviour, was proposed by Åström et al. [16]. A pressure profile was derived from the measured film thickness using deconvolution with the elastic deformation kernels. The only assumption then made is regarding the specifics of the deformation, which for standard materials is generally elastic and is known to be accurately described by the semi-infinite half space deformation added to an undeformed shape. Åström used the approach to determine pressure fluctuations induced in grease lubricated contacts. A disadvantage is that the deconvolution problem is poorly conditioned and small errors (noise) in the film thickness input lead to large errors in the computed pressures. Hence the pressure distribution has a limited accuracy, which calls for special measures in the deconvolution such as averaging. Examples of the extension and applications of the method are [17,18].

In this paper the method is further developed and it is shown how, benefiting from today's accurate measurement and computational methods, it is now possible to extract detailed high quality pressure information. The first step is to obtain high resolution film thickness data. However, rather than using this data as direct input for a pressure computation as in [17,18] the next step is to compute a theoretical very high resolution pressure and film thickness profile for approximately the same conditions. These two profiles are used as a reference. The film thickness profile aids in positioning the measured profile. Subsequently, from the film thickness difference a pressure difference is obtained by deconvolution.

The last task is one of filtering, to reduce the noise originating from the measurement error and the positioning error, that has been amplified by the deconvolution. Here the challenge is to remove high frequency fluctuations, without changing the pressure spike distribution, which is a high frequency perturbation itself. As such the smallest amount of filtering should be chosen. It was observed that the pressure spike shape was relatively constant over a part of a circle, and only averaging of the data over this circle segment was applied. The noise level in the obtained pressure spike profiles is amazingly low.

2. Measurement

The film thickness measurements were obtained by employing a high pressure ball on disk test rig that allows mapping of the film thickness distribution inside a point EHL contact, based on interferometry [12]. The rig consists of a microscope with a camera and an EHL simulator. The EHD film is formed between a steel ball and a glass disk coated by a chromium layer. Both surfaces can be driven independently by a servo motor with an attached gear box. The imaging unit is based on a conventional microscope with episcopic illumination equipped by a xenon light source and a digital camera. For more details concerning the apparatus see [12].

Inside the EHL contact, the bottom surface (the glass disk with the chromium layer) works as a splitter. As a result, a fraction of the light is reflected from this layer and the other part is reflected from the steel ball. The lubricant film thickness between these two surfaces introduces an optical path difference (OPD) that causes interference. If white light is used the maximum OPD can be approximately 2 μm to interfere. Because white light represents a wide band of wavelengths, not only the intensity but also the colour is changing as the OPD increases. This causes the typical interference patterns observed in EHL contacts.

Commonly, when measuring a smooth contact under steady state conditions, a digital camera with a low frame rate is used with an exposure time of approximately 10 ms. During this time all effects like roughness, impurities or dynamic behavior are averaged into a final image. If the speed is 0.5 m/s, a small spot in the actual field of view moves by 5000 μm during the exposure time. Therefore, it is difficult to observe all the effects that influence the final image. In this study a different approach is used. Instead of the standard frame rate, a high-speed camera was

employed. Measurements were performed by acquiring a series of one hundred frames with an exposure time of 10 μs and a frame rate of 8000 fps.

Afterwards, the frames are combined in the computer by making a selection of typically the 30 best images. The whole process is automated, by comparing the reference and the actual frame histogram and the centerline slices. Only frames with the highest correlation to the reference image are used. The final image is an average of a similar time sequence of 12 ms as in the case of the standard camera. Averaging has a positive effect on the noise level. Practical RMS values of small wavelength components in the final image are below 0.5 nm.

The evaluation of the interference pattern is based on a colorimetric interferometry method. The role of this method is to analyze the link between a particular color and the film thickness value. The color is described in a Lab color space which has the benefit that the set of color values and film thickness values can be represented by a smooth curve. For calibration monochromatic and chromatic (white light) images of the same static contact are necessary. The monochromatic light is used for the determination of the deformed ball shape to make a precise connection between color and film thickness value. For the evaluation a color matching algorithm is used to find the appropriate coordinates in the calibration space to give film thickness values for every point of the measured interferogram. For further details the reader is referred to [19].

The film thickness was corrected for the change in refractive index by employing a Hertzian pressure distribution. The correction procedure followed the steps presented in [12].

3. EHL reference solution

For the reference theoretical solution a standard EHL model is used. The two dimensional Reynolds equation reads:

$$\frac{\partial}{\partial x}\left(\frac{\rho h^3}{12\eta u_m}\frac{\partial p}{\partial x}\right)+\frac{\partial}{\partial y}\left(\frac{\rho h^3}{12\eta u_m}\frac{\partial p}{\partial y}\right)-\frac{\partial \rho h}{\partial x}=0 \quad (1)$$

The density pressure relation is according to Dowson Higginson, the viscosity pressure relation is according to Roelands. The film thickness equation is given by

$$h(x,y)=h_0+\frac{x^2}{2R_x}++\frac{y^2}{2R_y}+\frac{2}{\pi E'}\int_{-\infty}^{+\infty}\int_{-\infty}^{+\infty}\frac{p(x',y')\,dx'\,dy'}{\sqrt{(x-x')^2+(y-y')^2}} \quad (2)$$

and, the force balance equation is

$$\int_{-\infty}^{\infty}\int_{-\infty}^{\infty}p(x,y)\,dx\,dy=w \quad (3)$$

The equations were made dimensionless, discretised using a second order discretization, and solved using Multilevel techniques [20,21]. The application to the EHL point contact problem is extensively described in [22]. The method allows a simple and fast computation of the film thickness and pressure reference solution with very small grid spacing in a short time on a small scale computer.

As the solutions are used as reference solutions, the convergence was prolonged to obtain residuals less than 10^{-10}. With this precision, typical computing times for a solution of 2049^2 points are 15 min on a standard PC. The computational domain used was $-4.5\le X\le 1.5$ and $-3\le Y\le 3$. From the resulting pressure and film thickness distributions, only the central part was used: $-1.5\le X\le 1.5$ and $-1.5\le Y\le 1.5$. Fig. 1 shows an example of a detailed pressure distribution. Please note that the pressure spike is hardly visible in this graph. Consequently, the pressure difference has been used in subsequent graphs. This is the difference between the 'measured' or calculated pressure and the Hertzian distribution. The loading case is taken from experimental input conditions as listed in Table 1.

The Moes dimensionless parameters [28] characterizing this case are $M=265$ and $L=6.3$. The corresponding deformed ball

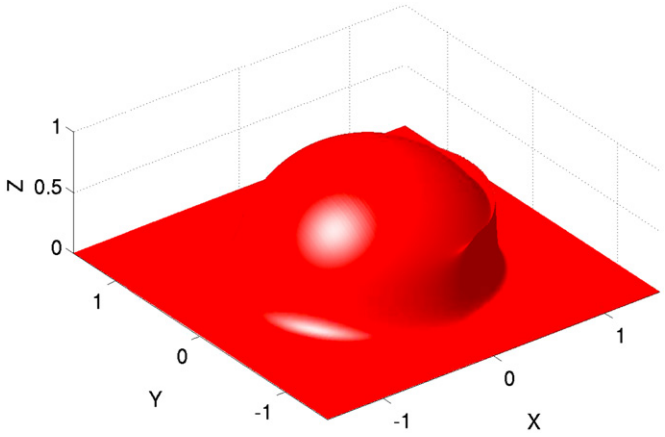

Fig. 1. Pressure distribution for $M=265$, $L=6.3$.

Table 1
Operating conditions and HPO200 lubricant data at 25 °C.

u_m	0.4 m/s
$R_x=R_y$	12.7 mm
E'	124 GPa
w	81 N
p_h	0.72 GPa
a	232 μm
η_0	70 mPa s
α	20.5 Gpa^{-1}

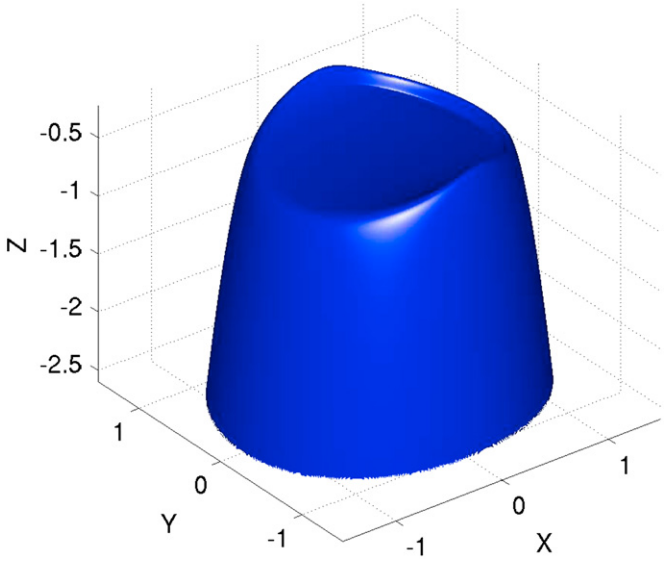

Fig. 2. Film thickness distribution for $M=265$, $L=6.3$, the Z-axis is amplified by a factor of 10.

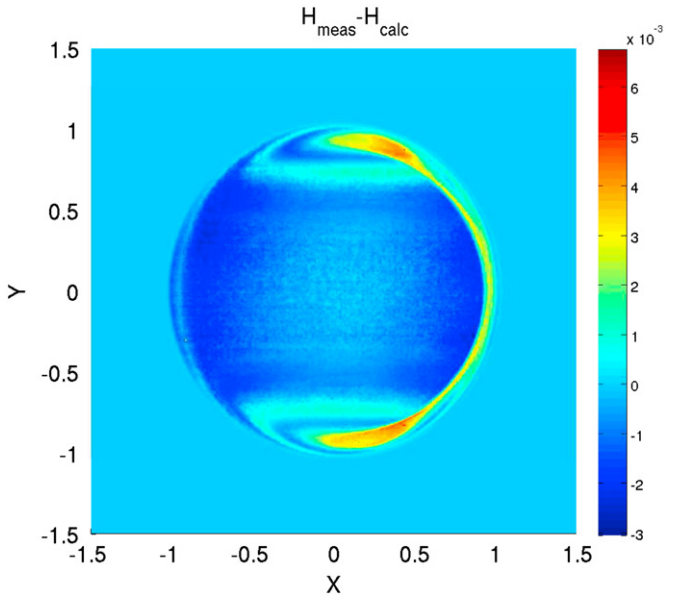

Fig. 3. Film thickness difference distribution for $M=265$, $L=6.3$.

geometry is plotted in Fig. 2. The Z-axis has been scaled by a factor of 10.

4. Fitting

The similarity between the measured and computed solution allows for a very precise positioning of the measured solution, along the three axes X, Y and Z. In a first step the measured data is converted to the dimensionless coordinates X, Y and film thickness H. Then the data is corrected for rotational misalignment and resampled to obtain the same mesh as the computed solution. A next step involves optimisation of the measured data position in X and Y direction to minimize the difference with the computed data. Finally the measured and computed data are subtracted and areas far outside the contact circle set to zero. An example of a film thickness difference distribution is shown in Fig. 3. Note that this is the difference between measured and computed film thickness. The film thickness difference is at least one order of magnitude smaller than the film thickness itself. Hence the symmetry of the difference graph says much about the quality of the original measurement.

5. Deconvolution

The deformation kernels for an elastic half-space are well know [23]. The problem resides in the amplification of all measurement and fit errors, as the inverse problem is very badly conditioned.

The elastic deformation d is given by

$$d(x,y)=\frac{2}{\pi E'}\int_{-\infty}^{+\infty}\int_{-\infty}^{+\infty}\frac{p(x',y')\,dx'\,dy'}{\sqrt{(x-x')^2+(y-y')^2}} \tag{4}$$

which reads in its discretised form:

$$d_{i,j}=\sum_k\sum_l K_{i,j,k,l}\,p_{k,l} \tag{5}$$

where K is the discretised elastic deformation kernel. The equation shows that the deformation in each point (i,j) depends on the pressure in all points (k,l). The inverse computation, i.e. the deconvolution, requires solving the integral (Fredholm) equation. With the use of Fast Fourier Techniques [24–26] or MultiLevel Multi-Integration techniques [21,22,27] this is no longer a computationally expensive task. However, this inverse problem, is poorly conditioned. The smaller and more localised the film thickness difference, the smaller and more localised the pressure difference. Furthermore, a localised solution will have a better condition number and the experimental noise amplification will be limited. As such the use of a reference solution allows a reduction of the 'fit' error, but also limits the amplification of the measurement noise.

6. Pressure spike averaging

In spite of all the care taken in the previous sections the pressure distribution when added to the numerically calculated distribution remains rather noisy as is shown in Fig. 4 depicting the center line pressure distribution.

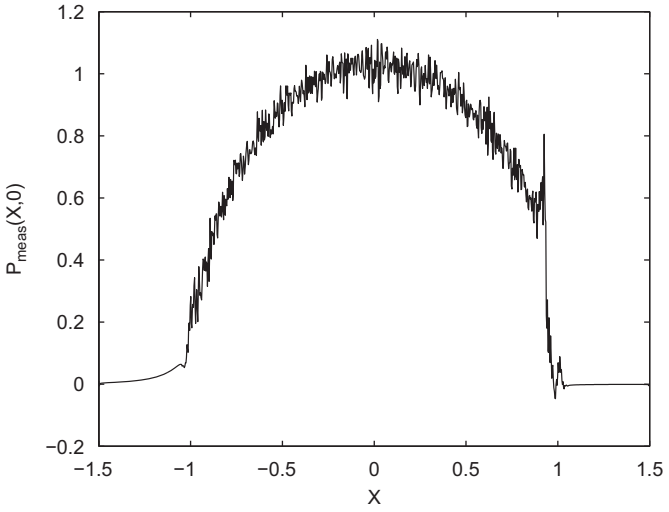

Fig. 4. 'Measured' pressure distribution along the center line $P(X,Y=0)$, $M=265$, $L=6.3$.

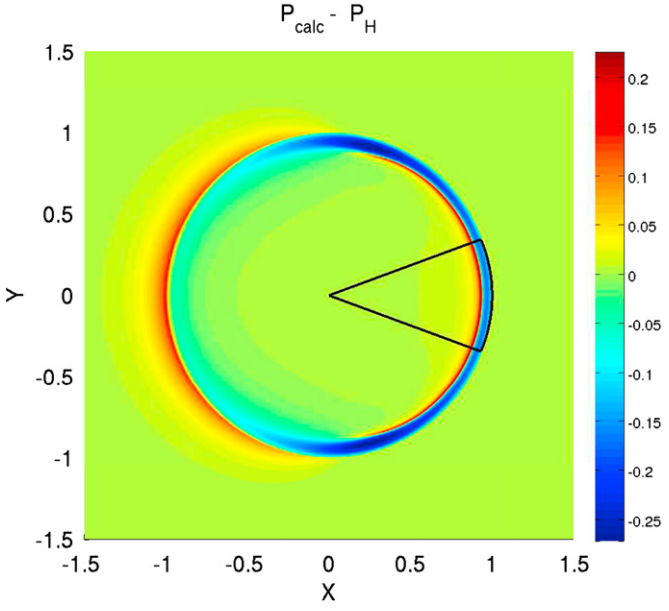

Fig. 5. Top view of computed pressure difference with Hertz and the arc over which averaging is applied. $M=292$, $L=6.9$.

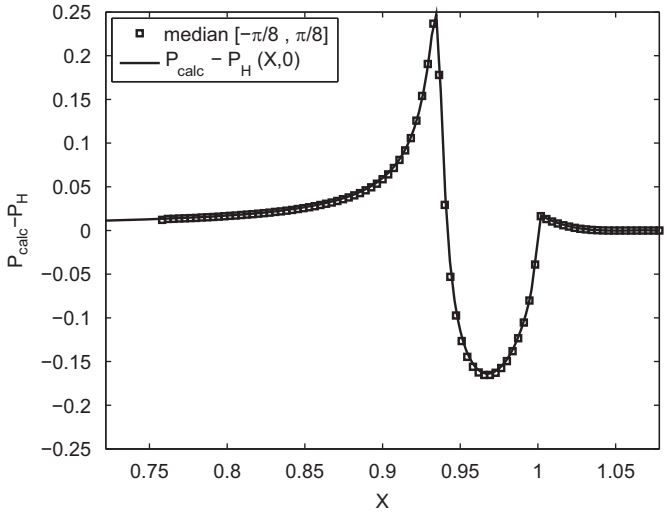

Fig. 6. Center line computed pressure spike shape (drawn) and arc-averaged pressure spike shape (squares) compared with Hertz distribution, $M=292$, $L=6.9$.

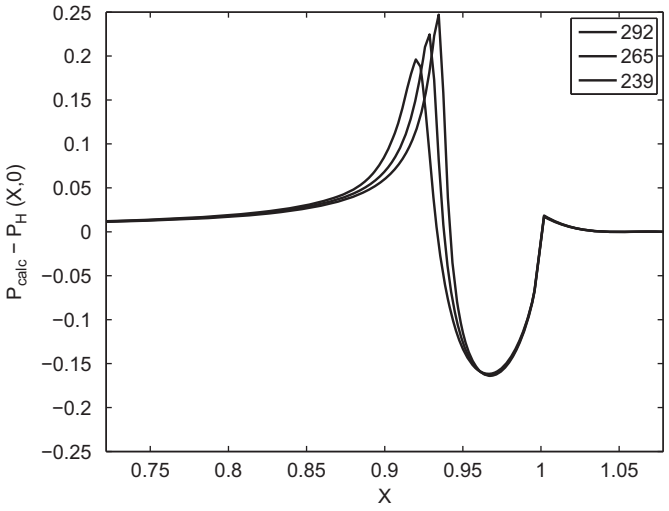

Fig. 7. Computed pressure spike shape compared with Hertz distribution for the three M values, M increases from left to right.

As a result some noise reduction is required, however, in order to limit the filtering influence on the pressure spike shape, only averaging is used. Fig. 5 shows the calculated pressure difference that is the calculated pressure minus the Hertzian pressure. From this figure it can be observed that the pressure variations exhibit a circular symmetry. This is true in the inlet as well as in the outlet as in the pressure spike region. As such averaging over a circular arc in the pressure spike zone was applied, see Fig. 5. The thin white line, inside the circle, near the exit of this figure, represents the positive pressure difference, in this case the pressure spike!

Fig. 6 shows the computed pressure spike shape on the central line $Y=0$ (drawn) and averaged pressure spike shape over the circular arc (squares).

The averaging was performed parallel to the 'best fit circle', averaging from R to $R+\delta R$, see the white pie-shaped area in Fig. 5. The averaging was performed over an arc from $-\pi/8$ to $\pi/8$.

This figure shows that the two shapes are very similar and consequently the same arc averaging was applied on the 'measured' pressure distribution.

A numerical mesh convergence check showed that, for the current operating conditions, the spike height does not depend on the mesh size.

7. Reference influence

The current procedure of extracting the pressure spike shape relies heavily on the use of a reference pressure and film thickness distribution. The current section investigates the influence of this reference solution. As claimed in previous sections, the reference solution only facilitates the fitting, thereby reducing the noise, as such it should not influence the shape of the pressure distribution nor the spike shape. To check this influence three different reference cases were computed: nominal $M=265$ $L=6.3$, low load $M=239$ $L=5.9$ and high load $M=292$ $L=6.9$. Fig. 7 shows the center line pressure spike shape compared to the Hertz solution for all three cases. It can be seen the pressure spike height and its position vary significantly while varying the operating conditions by only $\pm 10\%$.

In spite of these variations in the references, the arc averaged 'measured' spike shape using the three references are very similar as is shown in Fig. 8. As such it is concluded that minor variations in the operating conditions between measurement and computation, do not influence the 'measured' pressure significantly.

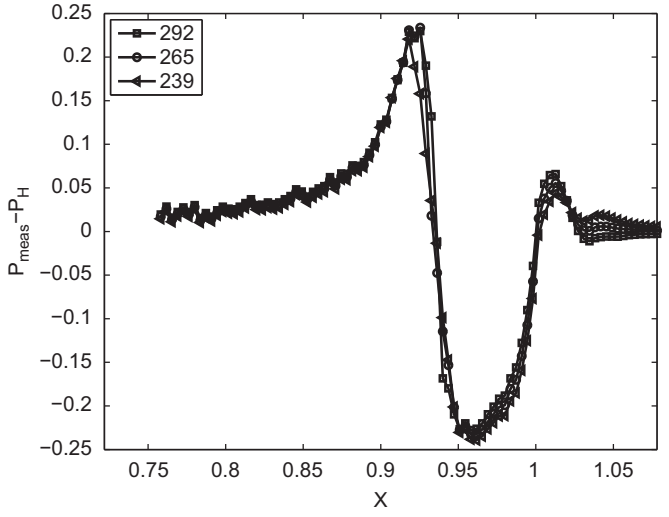

Fig. 8. Arc-averaged 'measured' pressure spike shape, using three different references.

It should be noted that none of the assumptions used to generate the reference solution affect the 'measured' pressure distribution! This can be most easily understood if imagining that the reference solution is the Hertzian dry contact solution. This choice would increase the noise, but not alter the pressure distribution. The only fundamental assumption used to obtain the "measured" pressure distribution is the linear elastic deformation!

8. Shear stress

The most interesting lubricant parameter is without a doubt the maximum shear stress attained in the pressure spike region. The shear stress in a thin film is given by

$$\tau_{zx}=\frac{1}{2}\frac{\partial p}{\partial x}(2z-h)+(u_2-u_1)\frac{\eta}{h} \tag{6}$$

Using the Hertz parameters this equation can be written in a dimensionless form as

$$\overline{\tau}_{ZX}=\frac{1}{2}\frac{\partial P}{\partial X}(2Z-H)+SRR\frac{\lambda\overline{\eta}}{12H} \tag{7}$$

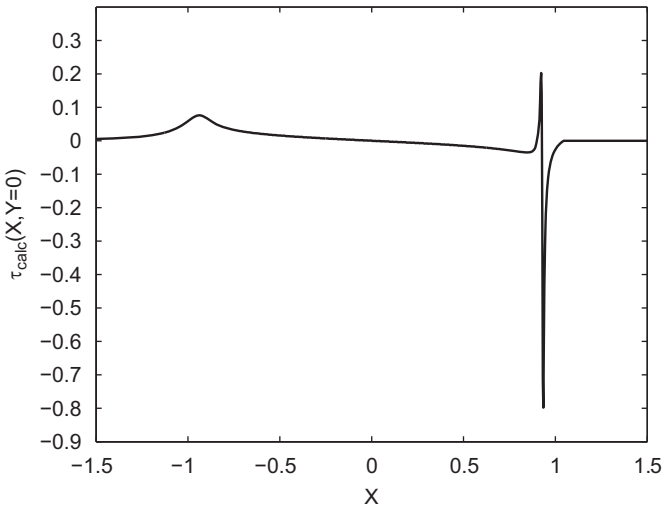

Fig. 9. Computed center line upper surface dimensionless shear stress, under pure rolling.

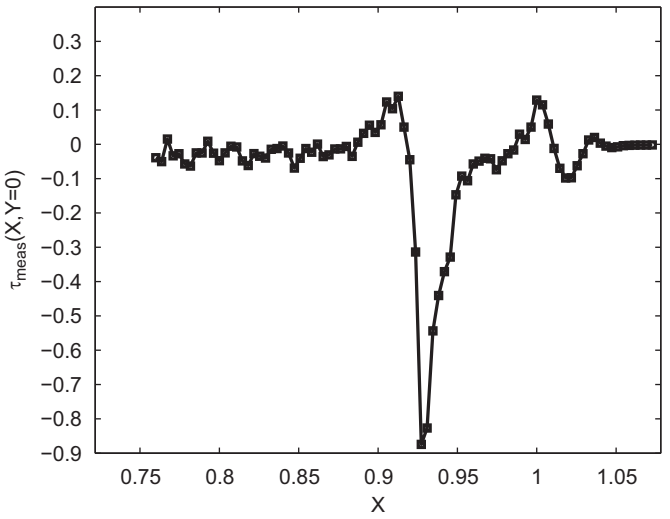

Fig. 10. Detail of the 'measured' dimensionless shear stress in the pressure spike zone.

The following relation links the dimensionless shear stress to the dimensional shear stress:

$$\tau_{zx} = \frac{p_h a}{R_x}\overline{\tau}_{ZX} \tag{8}$$

and the λ parameter is the same as used in the dimensionless Reynolds equation, see [22]. It is defined as

$$\lambda = \frac{12\eta_0 u_m R_x^2}{p_h a^3} \tag{9}$$

Fig. 9 shows the center line upper surface shear stress as a function of X: $\overline{\tau}_m(X,Y=0,Z=H)$.

From this figure it can be observed that the maximum shear stress occurs in the pressure spike zone, but that a non-negligible shear stress occurs in the inlet zone.

Finally, the 'measured' shear stress is computed, using the measured film thickness distribution and multiplying by the derivative of the 'measured' pressure distribution, see Fig. 10. To reduce the noise, arc averaging for the pressure spike shape was used, as explained previously.

Although the 'measured' shear stress is noisy, due to the pressure derivative, the qualitative shape is the same as computed. Moreover, quantitatively, the maximum and minimum values are very close to the computed ones, 'measured': 0.14, −0.87, computed: 0.20, −0.80. The Hertzian parameters for these operating condition are p_h=0.72 GPa, a=232 μm and R_x=12.7 mm. This gives a factor $p_h a/R_x$=13.2 MPa. The maximum value of the 'measured' shear stress in the pressure spike zone is τ_m=11.4 MPa. Hence, as the computed pressure distribution stems from a Newtonian calculation, it can be concluded that the lubricant operates in or close to its Newtonian range.

9. Influence of sliding speed

The current section analyses the influence of the slide to roll ratio on the pressure spike shape. Five film thickness distributions for pure rolling and for 5% and 10% slide to roll ratios were measured. The pressure spike shapes for pure rolling and 10% sliding are shown in Fig. 11. For 0% sliding, the maximum spike pressure is 0.51 ± 0.014 GPa. For 10% sliding the maximum pressure was found as 0.48 ± 0.014 GPa. These results indicate a small but significant difference between the two cases.

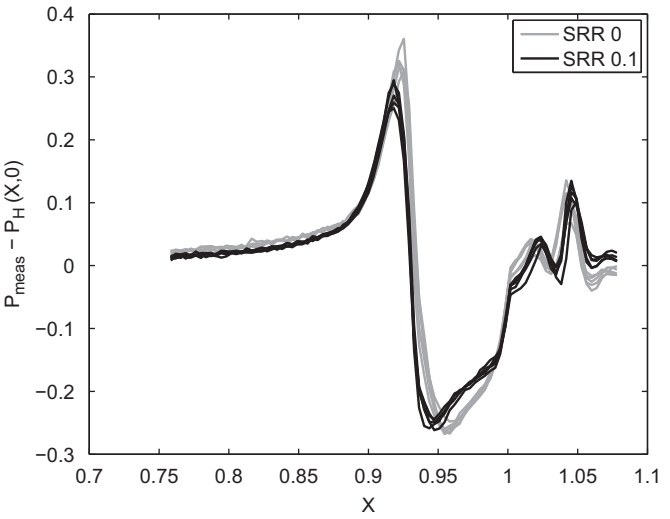

Fig. 11. Pressure spike shape (difference with Hertz) as a function of the slide to roll ratio, 0% (grey) and 10% (black).

Furthermore, there is a distinct shift in the spike position, between the 0% and the 10% sliding cases.

However, the five 5% measurements clouded the issue to some extent. The maximum spike height was the same as for 0% in two cases and the same as for 10% in two other cases. Only in one case an intermediate value was found.

The analysis of the shear stress distribution under sliding conditions will be undertaken in a future paper.

10. Discussion

The pressure spike height obtained in the previous section is significantly higher than the first measurements made, and also higher than the computed value. It is possible that small variations of the operating conditions can explain this phenomenon. Another possible explanation resides in the cavitation zone: the deconvolution generates significant pressure oscillations in this zone, in spite of the arc averaging. It seems that in the second series of measurements these oscillations are twice as pronounced. Finally, the choice of the Roelands viscosity pressure

relation is known to result in lower pressure spikes compared to the Barus equation.

Another point is that the authors have not made (recursive) corrections for the refractive index – pressure dependence, as this influence will have a global character. The local film thickness variations indicating the pressure spike should be only moderately affected. furthermore, the 5% slide to roll results be explained by a slide to roll ratio that on average is 5%, but oscillates between, say, pure rolling and 10% sliding. Finally, additional measurements are required to study the influence of the slide to roll ratio on the 'measured' shear stress.

11. Conclusion

This paper shows that it is possible to extract high quality pressure (spike) information from high quality film thickness measurements. To minimise the noise on the pressure (spike) signal, different necessary operations are detailed, such as the use of an H and P reference solution and arc averaging. It was shown that the reference solution should have similar operating conditions, but not necessarily identical ones. The resulting pressure spike profiles are amazingly detailed, and display very little noise.

For pure rolling and the current operating conditions, very sharp pressure spikes were obtained. Their height was similar to, or exceeded, the computed pressure spike height. As the computation uses a Newtonian model, one can conclude that the lubricant operates in or close to the Newtonian regime.

For the current oil and operating conditions, the 10% sliding generated a slight, but significant, reduction in the pressure spike height, as well as a shift to the left in the spike position.

Measurements using a higher resolution camera, combined with a finer reference computation, should be performed to see if under pure rolling conditions the measured pressure spike is indeed higher than the computed one. These measurements should then be compared to computed pressure distributions using both the Barus and Roelands viscosity pressure relation.

Using measurement at different rolling velocities and different temperatures, allows one to scan the maximum shear stress behaviour of the oil as a function of the pressure and temperature. As the measurements and computations are not very time consuming, a relatively complete map (p_{spike},T) could be obtained in a single day. This map should be compared to classical rheological measurements to quantitatively validate the proposed method.

Acknowledgment

The experimental part of this work was performed at CEITEC – Central European Institute of Technology with its research infrastructure supported by the project CZ.1.05/1.1.00/02.0068 financed from European Regional Development Fund.

References

[1] Bridgman PW. The physics of high pressure. New York: Dover; 1931.
[2] Bair S. High pressure rheology for quantitative elastohydrodynamics. Elsevier Tribology Series; 2007.
[3] Jacobson BO. A high pressure-short time shear strength analyser for lubricants. ASME Journal of Tribology 1985;106(2):220–3.
[4] Jacobson BO. Rheology and elastohydrodynamic lubrication, vol. 19. Elsevier Tribology Series; 1991.
[5] Johnson KL, Tevaarwerk S. Shear behaviour of elastohydrodynamic oil films. Proceedings of Royal Society A 1977;356:215–38.
[6] Cameron A, Gohar R. Theoretical and experimental studies of the film in lubricated point contacts. Proceedings of Royal Society A 1966;331:520–36.
[7] Foord CA, Wedeven LD, Westlake FJ, Cameron A. Optical elastohydrodynamics. Proceedings of the Institution of Mechanical Engineers 1969;184:487–505.
[8] Johnston GJ, Wayte RW, Spikes HA. The measurement and study of very thin lubricant films in concentrated contacts. Tribology Transactions 1991;34:187–95.
[9] Felix-Quinonez A, Ehret P, Summers JL. On three-dimensional flat-top defects passing through an EHL point contact: a comparison of modeling with experiments. ASME Journal of Tribology 2005;127(1):51–60.
[10] Choo JW, Glovnea RP, Olver AV, Spikes HA. The effects of three-dimensional model surface roughness features on lubricant film thickness in EHL contacts. ASME Journal of Tribology 2003;125(3):533–42.
[11] Larsson PO, Larsson R, Jolkin A, Marklund O. Pressure fluctuations as grease soaps pass through an EHL contact. Tribology International 2000;33(3–4):211–6.
[12] Krupka I, Hartl M, Poliscuk R, Cermak J, Liska M. Experimental evaluation of EHD film shape and its comparison with numerical solution. ASME Journal of Tribology 2000;122(4):689–96.
[13] van Leeuwen H. The determination of the pressure-viscosity coefficient of a lubricant through an accurate film thickness formula and accurate film thickness i measurements. Proceedings of the Institution of Mechanical Engineers: Journal of Engineering Tribology 2009;223:1143–63.
[14] Paul GR, Cameron A. High pressure and shear response using the rotating optical micro-viscometer. Proceedings of the Royal Society A 1972;331:171.
[15] Wong PL, Lingard L, Cameron A. High pressure and shear response using the rotating optical micro-viscometer. In: Proceedings of the Leeds–Lyon symposium on tribology; 1995. p. 199–205.
[16] Åström H, Venner CH. Soap thickener induced local pressure fluctuations in a grease-lubricated elastohydrodynamically point contact. Proceedings of the Institution of Mechanical Engineers 1994;208:191–8.
[17] Jolkin A, Larsson R. Determination of Lubricant compressibility in EHL conjunctions using the Hybrid technique. in: Proceedings of the Leeds–Lyon symposium on tribology; 1999. p. 589–96.
[18] Lord J, Jolkin A, Larsson R, Marklund O. A hybrid film thickness evaluation scheme based on multi-channel interferometry and contact mechanics. Journal of Tribology 2000;122:16–22.
[19] Hartl M, Krupka I, Liska M. Elastohydrodynamic film thickness mapping by computer differential colorimetry. Tribology Transactions 1999;42(2):361–8.
[20] Brandt A. Multi-level adaptive solutions to boundary value problems. Mathematics of Computation 1977;31(2):333–90.
[21] Brandt A, Lubrecht AA. Multilevel matrix multiplication and fast solutions of integral equations. Journal of Computational Physics 1990;90(2):348–90.
[22] Venner CH, Lubrecht AA. Multilevel methods in lubrication, vol. 19. Elsevier Tribology Series; 2000.
[23] Johnson KL. Contact mechanics. Cambridge University Press; 1986.
[24] Cooley CW, Tukey JW. An algorithm for the machine calculation of complex fourier series. Mathematics of Computation 1965;19:884–7.
[25] Stanley HM, Kato T. An FFT based method for solving rough surface contact. Mathematics of Computation 1997;19:884–7.
[26] Sainsot P, Lubrecht AA. Efficient solution of the dry contact of rough surfaces: a comparison of FFT and MG methods. Proceedings of the Institution of Mechanical Engineers 2011;225:441–8.
[27] Lubrecht AA, Ioannides E. A fast solution of the dry contact problem and the associated sub-surface stress field. Journal of Tribology 1991;113:128–33.
[28] Moes H. Lubrication and beyond. University of Twente web-site; 2000.